Epigenetic landscape of the H3K27me3 mark in macrophages transformed by *Theileria annulata*

Takaya Sakura[1,2,3,4], Shahin Tajeri[1,†], Zineb Rchiad[1,5], Hifzur R. Ansari[5], Abhinav Kaushik[5], Tobias Mourier[5], Arnab Pain[5,6], Michel Wassef[7,8,#] and Gordon Langsley[1,2,#]

[1]Biologie Comparative des Apicomplexes, Institut Cochin, Paris, France.

[2]Université de Paris, INSERM U1016, CNRS UMR 8104, France.

[3]Department of Molecular Infection Dynamics, Shionogi Global Infectious Diseases Division, Institute of Tropical Medicine (NEKKEN), Nagasaki University, Sakamoto, Nagasaki 852-8523, Japan.

[4]School of Tropical Medicine and Global Health, Nagasaki University, Nagasaki, 852-8523, Japan.

[5]Pathogen Genomics Laboratory, Biological and Environmental Sciences and Engineering (BESE) Division, King Abdullah University of Science and Technology (KAUST), Saudi Arabia.

[6]Research Center for Zoonosis Control, Global Institution for Collaborative Research and Education (GI-CoRE), Hokkaido University, Sapporo, Japan.

[7]Institut Curie, Paris Sciences et Lettres Research University, Sorbonne University, 75005 Paris, France.

[8]INSERM U934/CNRS UMR3215, 75005 Paris, France.

† Current address: Institute for Parasitology and Tropical Veterinary Medicine, Freie Universität Berlin, Berlin, Germany

[#] These authors contributed equally to this work

19 **Significance statement**

20 Tropical theileriosis is a major constraint to livestock production worldwide. Infection with *Theileria annulata*
21 induces the transformation of bovine leukocytes that subsequently exhibit similarities to human leukemia.
22 Long-term *in vitro* culture of transformed leukocytes attenuates their tumorigenic properties. The molecular
23 changes underlying this process are currently unclear. We focused on H3K27me3, a key histone tail post-
24 translational modification that regulates chromatin structure and gene expression, and compared its genomic
25 landscapes in virulent, highly disseminating macrophages *versus* attenuated macrophages with reduced
26 dissemination potential that are used as a live vaccine against tropical theileriosis. Western blot and ChIP-seq
27 revealed higher global levels of H3K27me3 and a striking broadening of its genomic distribution in attenuated
28 macrophages. To our surprise, this reconfiguration is not associated with major changes in gene expression
29 and attenuated cells appear to be less responsive to PRC2 inhibition, suggesting that large-scale broadening of
30 H3K27me3 does not systematically translate into increased PRC2-mediated silencing activity. Despite these
31 changes, H3K27me3 maintains the silencing of key tumor suppressor genes in both virulent and attenuated
32 macrophages. These findings shed light on the interplay between infection, the evolution of oncogenic
33 potential and reconfiguration of the chromatin landscape following attenuation of virulence.

Abstract

Theileria annulata and *T. parva* are obligate intracellular parasites that induce bovine leukocyte transformation, leading to uncontrolled proliferation and heightened dissemination of infected leukocytes, thus amplifying the parasite and enhancing its transmission. Early passage *T. annulata*-transformed macrophages are virulent, but virulence decreases with long-term passage and infected macrophages become attenuated for dissemination. Loss of dissemination is restored when TGF-β2-mediated signaling is re-established in attenuated macrophages, suggesting that genetic and/or epigenetic changes occurring within macrophages contribute to the attenuated phenotype. To elucidate the relationship between attenuation of dissemination and epigenetic dysregulation of *T. annulata*-transformed macrophages, we focused on one of the important repressive histone marks, tri-methylated lysine 27 of histone H3 (H3K27me3) catalysed by the Polycomb Repressive Complex 2 (PRC2). We found that the global level of H3K27me3 of *T. annulata*-infected macrophages is increased in attenuated macrophages compared to virulent macrophages. Chromatin immunoprecipitation sequencing (ChIP-seq) revealed that the genomic distribution of H3K27me3 is heavily remodeled from virulent to attenuated macrophages. In attenuated macrophages, many genes transition from a focal peak of H3K27me3 around the transcription start site to larger chromatin domains. But this transition is not paralleled by large-scale transcriptional downregulation. In addition, RNAseq analysis following PRC2 inhibitor treatment reveals that fewer genes are derepressed in attenuated macrophages than in virulent macrophages, suggesting that broader H3K27me3 profiles do not systematically translate into increased gene silencing activity. Our findings shed light on the mechanisms underlying the dysregulation of epigenetic

53 modifications in *Theileria*-induced leukocyte transformation and contribute to a better understanding of the

54 attenuation of tumor dissemination.

55 **Introduction**

56 Apicomplexan parasites *Theileria annulata* and *T. parva* are transmitted by ticks and infect bovine leukocytes,
57 causing tropical theileriosis primarily in Asian countries and East Coast Fever (ECF) in Africa[1,2].
58 Macroschizonts differentiated from tick-injected sporozoites induce tumorigenesis of infected leukocytes, and
59 dissemination of transformed leukocytes is mainly responsible for the pathology of these livestock diseases.
60 Despite the huge economic impact of this disease in the veterinary field, available vaccines suffer from several
61 drawbacks such as the requirement for quality control, cold chain[3,4]. In addition, parasites resistant to the
62 theileriacidal drug buparvaquone are emerging in endemic areas[5,6]. New vaccines and drugs are therefore
63 needed to control these widespread livestock diseases and to reduce their economic burden in endemic areas.
64 A specific feature of *T. annulata* and *T. parva* infections is the transformation of their host leukocytes that
65 allows the parasite population to grow due to uncontrolled host cell proliferation[7,8]. The mechanisms
66 underpinning *Theileria annulata*-mediated transformation – i.e., how parasites modulate host gene expression
67 and hijack their proliferation – rely on host-parasite interactions. For instance, the IκB kinase (IKK) complex
68 is recruited to the surface of the parasite resulting in nuclear factor kappa B (NF-κB) being constitutively
69 activated to induce expression of anti-apoptotic genes[9]. In addition, *Theileria* infection inhibits nuclear
70 translocation of p53, a well-known tumor suppressor, and blocks p53-driven expression of pro-apoptotic
71 genes[10,11]. Meanwhile, c-Jun N-terminal Kinase (JNK2) interacts with a GPI-anchored macroschizont surface
72 protein (p104), while JNK1 translocates to the nucleus to activate c-Jun to drive transcription of the matrix
73 metalloproteinase 9 (*mmp*9) gene and enhance tumor dissemination[12–14]. Parasite secreted peptidyl-prolyl
74 isomerase PIN1 also contributes to c-Jun stabilization that maintains the proliferative phenotype of *Theileria*-

75 infected leukocytes[15]. Subversion of host cell signal transduction pathways augments *c-myc*-driven

76 transcription of anti-apoptotic genes[16–18]. *Theileria* transformation therefore shares several similarities with

77 human carcinogenesis, where epigenetic (i.e., not involving changes of the DNA sequence) alterations

78 contribute to cancer development. For example, *Theileria*-induced tumor dissemination is regulated by

79 changes in TGF-β2 levels and dissemination of attenuated macrophages is restored by addition of exogenous

80 TGF-β2 consistent with a role for epigenetic regulation of cancer-related genes[19–21].

81 Many types of post-translational modifications on histone tails have been shown to regulate chromatin

82 dynamics and transcription[22]. Changes of the chromatin state have been reported in *Theileria*-infected

83 leukocytes. Tri-methylated lysine 4 of histone H3 (H3K4me3) is a mark correlating with active transcription

84 enriched upstream of the *mmp-9* gene in the *Theileria*-infected B-cell lymphosarcoma cell line (TBL3), and

85 transcriptional activation of *mmp-9* is associated with heightened tumor dissemination[23,24]. Tri-methylated

86 lysine 27 of histone H3 Histone H3 at lysine 27 (H3K27me3) is a key chromatin modification catalyzed by

87 the Polycomb Repressive Complex 2 (PRC2)[25]. H3K27me3 is associated with transcriptional silencing, acting

88 in part as a docking site for CBX containing PRC1 complexes. During embryonic development, H3K27me3

89 plays key a role in maintaining transcriptional silencing of developmental regulators[26]. Furthermore, the PRC2

90 complex is altered in several types of tumors, acting either as a tumor suppressor or an oncogene[27].

91 *Theileria annulata*-infected macrophages are fully transformed and as such can be maintained in culture

92 indefinitely. Early passage *T. annulata*-transformed macrophages are virulent (disseminating), but virulence

93 decreases with long-term (>300) passage and immortalized macrophages become attenuated for

94 dissemination[28,29]. In the present study, using the Polycomb-specific H3K27me3 histone mark as a paradigm,
95 we investigate the evolution of the epigenetic landscape between virulent and attenuated *T. annulata*-infected
96 macrophages. We show that the distribution of H3K27me3 in attenuated macrophages is profoundly altered
97 and attenuated cells become less responsive to PRC2 inhibition compared to virulent macrophages. However,
98 some tumor suppressor genes still respond to PRC2 inhibitor treatment. Our study therefore reveals profound
99 changes in the chromatin landscape that accompany the transition from virulent to attenuated states.

100 **Results**

101 ***Theileria annulata* parasites within transformed host leukocytes are not stained by a H3K27me3-**
102 **specific antibody.**

103 When comparing the amino acid sequence of the tail of histone H3 between various parasite species, we found
104 that the amino acid sequence surrounding Lys27 is highly conserved between mammals and *Plasmodium*
105 *falciparum* and *Toxoplasma gondii* (Fig. 1a). Accordingly, H3K27me3 is present in *T. gondii* tachyzoites and
106 has been detected in sexual stage II gametocytes in *P. falciparum*[30–33]. We noticed that there's an S>T change
107 at position 28 of *Theileria* parasite histone H3, raising the question whether H3K27 is tri-methylated in
108 *Theileria* species. As expected, immunofluorescence analysis using an antibody specific for H3K27me3
109 stained bovine host nuclei, whereas *Theileria* nuclei were not stained (Fig. 1b). Whether this is due to absence
110 of the mark and/or a failure of the antibody to recognize it (due to the H3S28>T change) is unclear. By
111 contrast, specific antibodies to H3K4me3 decorated both parasite and host cell nuclei. Since H3K27me3 is not

112 detected in the parasite by the antibody we used, the following analyses of H3K27me3 reflect only the bovine

113 histone mark.

114 **Global levels and distribution of H3K27me3 are altered in attenuated macrophages.**

115 The fact that attenuated macrophages have a low dissemination potential led us to hypothesize that oncogenes

116 activated as a consequence of *Theileria* infection might be transcriptionally downregulated through

117 mechanisms promoting a repressed chromatin state. To this end, we quantified H3K27me3 abundance in the

118 nuclear fraction of both virulent and attenuated macrophages (Fig. 2a). The amount of H3K27me3 was higher

119 in attenuated macrophages than in virulent macrophages, whereas H3K4me3 was lower in attenuated

120 macrophages. Interestingly, the expression of EZH2, the main PRC2 catalytic subunit, appeared unchanged

121 between virulent and attenuated macrophages.

122 We next investigated the genome-wide distribution of these marks in *Theileria*-infected macrophages by

123 chromatin immunoprecipitation sequencing (ChIP-seq). *Drosophila melanogaster* chromatin was used as a

124 spike-in control in order to normalize the abundance of the histone marks[34]. Consistent with the increase in the

125 amount of H3K27me3 observed by immunoblotting, the density of the mark around transcriptional start sites

126 (TSS) was globally higher in attenuated than virulent macrophages (Supplementary Fig. S1). H3K27me3 was

127 also poorly correlated between virulent and attenuated macrophages at the genome-wide level (r=0.593 and

128 0.603 for replicates 1 and 2, respectively), contrasting with the high degree of H3K4me3 correlation (r=0.976

129 and 0.973 for replicate 1 and 2 respectively) (Fig. 2b). A large number of H3K27me3-positive genes were

130 specific to either virulent or attenuated macrophages, while very few differences were observed for

131 H3K4me3-positive genes (Fig. 2c). Strikingly, plotting the average H3K27me3 signal revealed that while the
132 mark was increased overall over the gene bodies of attenuated cells, its relative distribution around the TSS
133 was strikingly different between virulent and attenuated cells (Fig. 2d). In virulent macrophages, H3K27me3
134 showed a typical enrichment around the TSS. However, in attenuated macrophages, H3K27me3 enrichment
135 was no longer maximal at the TSS. Instead, the mark accumulated most prominently in intergenic regions
136 (upstream of TSS and downstream of transcription termination sites). This contrasts with H3K4me3 that
137 accumulated sharply around the TSS and showed a similar distribution pattern between virulent and
138 attenuated macrophages.
139 We further defined 3 clusters of genes according to H3K27me3 enrichment (Fig. 3a): virulent-positive (cluster
140 1), attenuated-positive (cluster 2), both positive (cluster 3). While virulent-specific H3K27me3 signal showed
141 a sharp enrichment around the TSS, attenuated-specific H3K27me3 signal showed a wide distribution around
142 the TSS of attenuated macrophages, with a maximal enrichment upstream of the TSS. This difference was
143 also obvious for genes showing H3K27me3 enrichment in both conditions (Fig. 3a). Average transcript levels
144 in virulent and attenuated macrophages for each H3K27me3 cluster showed no statistically significant
145 difference as a group, while differential gene expression analysis identified a subset of cluster 2 genes that
146 were downregulated in attenuated *versus* virulent macrophages (Fig. 3b)[35]. One of the genes highly enriched
147 for H3K27me3 in cluster 2 in attenuated macrophages is the Src Kinase Associated phosphoprotein 2
148 (SKAP2) that's associated with cell adhesion of macrophages[36]. It is covered by a large domain of H3K27me3
149 extending over 500 kb, in contrast to a low level concentrated at the TSS found in virulent macrophages (Fig.

150 3c), corresponding to the downregulation of SKAP2 in attenuated macrophages[35]. Peaks pattern of

151 H3K27me3 and H3K4me3 on the representative genes in other clusters, TBX5 (Cluster 1) and WNT3 (Cluster

152 3) were also visualized (Fig. 3c). Altogether, these data show that the attenuated phenotype is characterized

153 by a dramatic reconfiguration of H3K27me3 distribution.

154 **Limited effect of PRC2 inhibition on tumor-related phenotypes**

155 In light of the widespread re-distribution of H3K27me3 in attenuated cells, we next investigated the

156 requirement for the mark in the transformed and attenuated phenotypes. We treated both virulent and

157 attenuated macrophages with a specific PRC2 inhibitor (UNC1999) and its inactive analog (UNC2400)[37,38].

158 Ten days treatment with UNC1999 lead to an acute loss of H3K27me3 in both cell lines (Fig. 4a). We then

159 performed fibronectin-binding assays using the PRC2 inhibitor treated macrophages (Ref). Though attenuated

160 macrophages displayed lower binding activity compared with virulent macrophages, PRC2 inhibition did not

161 affect binding activity (Fig. 4b). We injected the PRC2 inhibitor treated macrophages into immune-

162 compromised Rag2/γC mice and then orally administrated PRC2 inhibitor for 3-weeks to evaluate if loss of

163 H3K27me3 impacts on formation of tumors *in vivo*. The parasite burden of each organ was quantified by the

164 amount of DNA corresponding to the *T. annulata ama-1* gene (TA02980). Similar to the fibronectin-binding

165 assay, there was no significant change resulting from PRC2 inhibition (Fig. 4c).

166 **H3K27me3-mediated gene repression is dampened in attenuated macrophages**

167 We next assessed gene expression changes following PRC2 inhibition in virulent and attenuated cells. For this

168 purpose, we performed RNA-seq on *Theileria*-infected macrophages treated with UNC1999 or UNC2400 for

169 10 days to identify the genes whose transcription is reactivated following loss of PRC2 activity. Due to the
170 repressive function of H3K27me3, PRC2 inhibition resulted in a majority of differentially expressed genes
171 (DEGs) being upregulated in both virulent and attenuated macrophages (Fig. 5a). Interestingly, the number of
172 upregulated genes in virulent macrophages was more than 2-fold higher than in attenuated macrophages,
173 suggesting that gene silencing is less dependent on PRC2 in attenuated macrophages. Twenty-one genes were
174 commonly upregulated in virulent and attenuated macrophages suggestive of a core function for H3K27me3-
175 mediated repression in *Theileria*-infected macrophages (Fig. 5b, Supplementary Fig. S2, S3, and
176 Supplementary Table S2). Gene ontology analysis also demonstrated that PRC2 retains its canonical function
177 of regulating genes related to embryonic development in virulent macrophages. However, enrichment for this
178 class of genes is no longer statistically significant in attenuated macrophages (Fig. 5c). This functional
179 difference in PRC2 inhibitor responsiveness between virulent and attenuated macrophages could be caused by
180 the difference of genome-wide distribution of H3K27me3 (Fig. 2b). Remarkably, some of the common PRC2-
181 repressed genes (Fig. 5d) include Granzyme A (GZMA) identified as a novel dissemination suppressor of
182 *Theileria*-transformed macrophages[35] and Follistatin (FST) known to reduce tumor invasiveness and
183 metastasis in breast cancer[39,40].
184 Overall, our analyses of the epigenetic landscape of *Theileria*-infected macrophages have uncovered a
185 dramatic reconfiguration of the H3K27me3 genomic pattern during the transition from the virulent to the
186 attenuated state. The histone mark adopts a broad pattern of genomic distribution reminiscent of the transition
187 from sharp to broad domains observed during development in the transition from the pluripotent to the

188 differentiated state[41]. This is paralleled by a reduced transcriptional response following PRC2 inhibition,
189 suggesting that this broad pattern may be less conducive to gene silencing and/or more resilient to PRC2
190 inhibition. Interestingly, silencing of some key tumor suppressor genes is preserved in attenuated
191 macrophages, highlighting the requirement for a minimally functional PRC2 complex.

192 **Discussion**

193 *Theileria* parasites modulate host leukocyte gene expression to induce uncontrolled leukocyte proliferation,
194 thereby favoring their own reproduction, as parasites are distributed to both daughter leukocytes following cell
195 division[42]. The unrestrained leukocyte proliferation and illicit dissemination within *Theileria*-infected animals
196 have several similarities with human carcinogenesis, and for this reason we focused on key post-translational
197 modifications of histone tails with established links to oncogenic phenotypes. We chose to map H3K4me3 and
198 H3K27me3 histone marks in virulent disseminating *T. annulata*-transformed versus attenuated macrophages
199 with dampened dissemination. As H3K27me3 is a key repressive mark we hypothesized that changes in its
200 genomic distribution could underlie some of the changes occurring during the attenuation processes. Indeed,
201 we observed that the distribution of H3K27me3 is dramatically reconfigured during attenuation. In virulent
202 macrophages, H3K27me3 preferentially accumulates around the TSS of developmental regulators (Fig. 5c),
203 while H3K27me3 in attenuated macrophages adopts a broader profile over large regions sometimes
204 encompassing multiple genes. Furthermore, H3K27me3 peaks on the DEGs between virulent and attenuated
205 macrophages also exhibited a similar distribution (Supplementary Fig. S4)[35].

206 Repressive histone marks are tightly related to heterochromatin structure, but just how methyltransferases
207 recognize specific sites in whole chromosomes is still not fully understood. Recently, it has been revealed that
208 phase separation of H3K9me2/3 and Heterochromatin Protein 1 (HP-1) drives heterochromatin formation and
209 fusion[43]. Moreover, the disordered region of CBX2, a subunit of the PRC1 complex can form condensates and
210 is important to maintain a transcriptionally repressed state[44,45]. Long-term oxidative stress also increases
211 H3K27me3 levels and attenuated macrophages exhibit elevated H_2O_2 production[46,47]. This suggests a potential
212 link between heightened oxidative stress and the widespread distribution of H3K27me3 in attenuated
213 macrophages. Given that follicular lymphoma harboring EZH2 mutations displays irregular H3K27me3
214 methylation, we looked at SNPs in the *ezh2* genes of virulent and attenuated macrophages. However, we could
215 find no evidence of any amino acid changes whether conferring a gain-of-function change or otherwise. Thus,
216 we checked our RNAseq data for *ezh2*-associated genes and only *phf19* displayed reduced expression in
217 attenuated macrophages, a reduction confirmed by qRT-PCR (Supplementary Fig. S5). Given the reduction in
218 *phf19* mRNA levels in attenuated macrophages is significant ($p = 0.0052$) one possibility is that reduced
219 levels of PHF19 might destabilize the PPRC2 to an extent that although EZH2 can still methylate K27, to a
220 large extent the complex doesn't repress all marked genes. Many *Toxoplasma* effector molecules localized in
221 the host nucleus have disordered regions that could contribute to the formation of phase-separated
222 compartments in the chromatin of host cells[48,49]. We did not elucidate whether and how *Theileria annulata*
223 infection alters the host cell epigenetic landscape and it is possible that the parasite secretes effector molecules
224 that might translocate to the host nucleus and reorganize bovine chromatin structure[50–52].

225 Interestingly, we found that this reconfiguration of H3K27me3 distribution is not associated to widespread
226 gene silencing and that fewer genes become de-repressed following PRC2 inhibition in attenuated cells than in
227 virulent macrophages. These observations suggest that this reconfiguration of H3K27me3 does not lead to a
228 globally increased PRC2 silencing activity. Why spreading of H3K27me3 does not lead to a more extensive
229 repression of transcription in attenuated macrophages is unclear, but we note that genes that gain H3K27me3
230 in attenuated macrophages are on average already lowly expressed in virulent cells (Fig. 3b). Previous studies
231 have shown that global increases in H3K27me3 can lead to complex effects on transcription that do not
232 necessarily result in a stronger repression of Polycomb target gene[53,54]. Interestingly however, PRC2 inhibitor
233 treatment led to the de-repression of three tumor suppressor genes *GZMA, PRF1* and *FST* in both virulent and
234 attenuated macrophages, indicating that H3K27me3 is required in maintaining their repressed state, thus
235 potentially contributing to the cancer-like phenotype of *Theileria*-induced transformation. This is consistent
236 with our observation that *GZMA* plays a role in tumor dissemination of *Theileria*-infected leukocytes and
237 human B-cell lymphomas[35]. The observation that genes silenced by PRC2 comprise both tumor suppressors
238 and oncogenes may explain the lack of an obvious effect of inhibiting PRC2 on the transformed phenotype.
239 Alterations of the chromatin state following host-parasite infection have also been reported in other contexts.
240 In particular, intracellular pathogens are capable of epigenetically modifying gene expression of infected host
241 cells by injecting effector molecules. *Legionella pneumophila* secretes the methyltransferase RomA into the
242 host cell to modify H3K14 acetylation and promote intracellular bacterial replication[56]. Amastigotes of
243 *Leishmania*, an obligate intracellular parasite, can induce epigenetic alterations of host macrophages, such as

244 DNA and histone modifications to promote pathogen survival and replication[57]. For instance, modulation of
245 host H3 acetylation and methylation by *Leishmania* amastigotes prevents NF-κB and NLRP3 inflammasome
246 activation, resulting in suppression of host immune responses[58,59]. The Apicomplexa parasite, *Toxoplasma*
247 *gondii* hijacks host cell signaling pathways and modifies the epigenetic state to prevent host cell apoptosis.
248 Recently, it was shown that *Toxoplasma* E2F4-associated EZH2 inducing Gene Regulator (TEEGR) activates
249 EZH2 and antagonizes NF-κB signaling by epigenetic repression in host cells[60]. However, the level of host
250 EZH2 protein did not change between virulent and attenuated macrophages (Fig. 2a) suggesting that other
251 mechanisms alter H3K27me3 distribution in *Theileria*-infected macrophages. Above we postulated that
252 reduced PHF19 expression might be one mechanism that could be directly tested by knocking down PHF19
253 levels in virulent macrophages to see if this induces abnormal spreading of H3K27me3 marks. Whether
254 *Theileria* plays an active role in modulating the H3K27me3 landscape of its host cell, or whether the changes
255 we observed are caused by changes in the chromatin regulatory properties of the host cell during the
256 attenuation process are important questions that will need to be addressed in future studies.
257

258 **Materials and Methods**

259 **Cell culture**

260 *Theileria annulata*-infected macrophages are the Ode virulent and attenuated lines corresponding to passage
261 53 and 309 [29,61]. These cells were maintained with RPMI medium supplemented with 10% fetal bovine serum
262 (FBS), 2 mM L-Glutamine, 100 U penicillin, 0.1 mg/ml streptomycin, and 4-(2-hydroxyethyl)-1-

263 piperazineethanesulfonic acid (HEPES) at 37°C with 5% CO_2.

264 **Immunofluorescence microscopy**

265 1×10^5 cells were centrifuged on glass slide with the Cellspin I (Tharmac) at 1,500 rpm for 3 min and fixed by

266 4% paraformaldehyde for 10–15 min at room temperature. Fixed cells were permeabilized with 0.2% Triton

267 X-100 for 10 min and blocked with 1% BSA for 30 min. These cells were incubated with primary antibodies

268 against H3K27me3 (1/1000, Cell Signaling) or H3K4me3 (1/1000, Cell Signaling) with parasite surface

269 protein p104 (1/1000, 1C12)[62] for 1 h at room temperature, sequentially stained with secondary antibodies

270 conjugated with Alexa 488 and Alexa 594 (1/1000, Molecular Probes) for 45 min at room temperature.

271 Stained cells were mounted in ProLong Diamond Antifade Mountant with DAPI (Thermo Fisher Scientific).

272 Stained cells were imaged by wide field Leica DMI6000 and these images were deconvoluted.

273 **Preparation of nuclear extracts**

274 We washed 0.5–2 × 10^7 *T. annulata*-infected macrophages and *D. melanogaster* S2 cells with phosphate-

275 buffered saline (PBS) once and subsequently suspended with Buffer A (10 mM pH7.9 HEPES, 5 mM $MgCl_2$,

276 250 mM sucrose, 0.1% NP40) supplemented with protease inhibitors and 1 mM DTT. After keeping on ice for

277 10 min, cell suspensions were centrifuged 8,000 rpm for 10 min at 4°C to collect cytosolic fraction. Pellets

278 were subsequently suspended with Buffer B (25 mM pH7.9 HEPES, 1.5 mM $MgCl_2$, 0.1 mM EDTA, 20%

279 Glycerol, 700 mM NaCl) supplemented with protease inhibitors and 1 mM DTT followed by sonication for 10

280 min on ice. Nuclear fractions were collected from supernatant of the centrifuged solutions (14,000 rpm for 15

281 min at 4 °C). Collected nuclear extracts were quantified by the Bradford protein assay.

282 **Immunoblotting**

283 Nuclear extracts were run by SDS-PAGE and transferred to nitrocellulose membrane (GE healthcare),
284 subsequently membranes were blocked with 5% (w/v) skimmed milk powder in PBS containing 0.1% Tween
285 20 (PBS-T) for 1 h at room temperature. Immune reactions were carried out using 1/2000 diluted monoclonal
286 rabbit anti-H3K27me3 or H3K4me3 antibodies (Cell signaling) or 1/50000 diluted monoclonal rabbit anti-H3
287 antibodies (Active motif) overnight at 4 °C as primary antibody. 1/5000 diluted HRP-labeled anti-rabbit
288 secondary antibodies (Santa Cruz) for 1 h at room temperature. Proteins were visualized with X-ray film or
289 ECL (Thermo Fisher Scientific) and imaged fusion FX (Vilber Lourmat). The H3 levels were used as a
290 loading control.

291 **Preparation of chromatin**

292 We cross-linked 1.5×10^7 cells by pre-warmed DMEM supplemented with 1% Formaldehyde, 15 mM NaCl,
293 150 μM EDTA, 75 μM EGTA, and 15 mM pH 8.0 Hepes for 10 min at room temperature with slow agitation
294 and then quenched formaldehyde with 125 mM Glycine for 5 min at room temperature. Following
295 centrifugation at 1000 rpm for 10 min at 4 °C, cells were with cold PBS once. Washed cells were suspended
296 with 1 ml Buffer 1 (50 mM pH7.5 Hepes-KOH, 140 mM NaCl, 1 mM EDTA, 10% glycerol, 0.5% NP40,
297 0.25% Triton X-100) supplemented with protease inhibitors (PMSF, aprotinin, leupeptin, pepstatin) and
298 rocked at 4 °C for 10 min. Following centrifugation at 1500 rpm for 5 min at 4 °C, cells were resuspended
299 with 1 ml Buffer 2 (10 mM pH8 Tris, 200 mM NaCl, 1 mM EDTA, 0.5 mM EGTA) supplemented with
300 protease inhibitors (PMSF, aprotinin, leupeptin, pepstatin) and rocked at room temperature for 10 min. Cells

301 were centrifuged at 1500 rpm for 5 min at 4 °C and resuspended 1.3 ml Buffer 3 (10 mM pH8 Tris, 1 mM

302 EDTA, 0.5 mM EGTA, 0.5% N-lauroyl-sarcosine) supplemented with protease inhibitors (PMSF, aprotinin,

303 leupeptin, pepstatin). Suspended cells were sonicated using the Bioruptor (Diagenode) with the setting (high,

304 30-sec intervals for 30 min) and chromatin were collected after centrifuge at 14,000 rpm for 10 min at 4 °C.

305 The size of reverse cross-linked DNA was 300–500 bp determined by DNA electrophoresis. Each chromatin

306 sample was quick-frozen in liquid nitrogen and stored at -80 °C.

307 **Chromatin-DNA quantitation.**

308 We mixed 20 μl of chromatin with 180 μl of $T_{50}E_{10}S_1$ (50 mM Tris pH 8.0, 10 mM EDTA, 1% SDS) at 65°C

309 for overnight for reverse-crosslinking. We added RNase A to chromatin samples and then incubated them for

310 1 h at 37°C to eliminate RNA from samples. Samples were incubated with Protease K for 1 h at 55°C. Extract

311 samples were mixed with phenol:chloroform:isoamyl-alcohol and sequentially added 20 μg glycogen. Purified

312 chromatin-DNA were collected by Ethanol/NaCl precipitation and their concentration were determined with a

313 Qubit Fluorometer (Thermo Fisher Scientific).

314 **Chromatin-immunoprecipitation (ChIP)**

315 Dynal magnetic beads (Thermo Dynabeads Protein A: 10001D) were incubated with 20 μl of H3K4me3 or

316 H3K27me3 antibodies for 8 hours at 4 °C. We prepared chromatin solution mixed with 20 or 10 μg chromatin

317 for H3K4me3 or H3K27me3 antibodies with 5% S2 chromatin in incubation buffer (3% Triton X-100, 0.3%

318 sodium deoxycholate, 15 mM EDTA) supplemented with protease inhibitors (PMSF, aprotinin, leupeptin,

319 pepstatin). These chromatin solutions were mixed with antibodies coupling beads and incubated on rotator for

320 overnight at 4°C. Each bead was washed 6 times by ice-cold RIPA (50 mM Hepes-KOH pH7.5, 10 mM

321 EDTA, 0.7 % sodium deoxycholate, 1 % NP-40, 0.5 M LiCl) supplemented with protease inhibitors (PMSF,

322 aprotinin, leupeptin, pepstatin) and additionally washed Tris-buffer (10 mM Tris pH8.0, 1 mM EDTA, 50 mM

323 NaCl). We eluted chromatin by 200 µl of $T_{50}E_{10}S_1$ (50 mM Tris pH 8.0, 10 mM EDTA, 1% SDS) at 65°C for

324 30 min by shaking at maximum speed. Beads were centrifuge at 14,000 rpm for 1 min and placed on the

325 magnetic stand. After revers-crosslinking described above, purified chromatin-DNA concentration was

326 determined with a Qubit Fluorometer (Thermo Fisher Scientific).

327 **ChIP-Seq analysis**

328 We mapped all precipitated read to *Bos taurus* (bosTau8) and *D. melanogaster* (dmel5.41) genome by

329 bowtie2-2.1.0 and processed generated files by Samtools[63,64]. Read normalization factors were calculated from

330 the number of mapped reads to the *D. melanogaster* genome according to the spiking methods

331 (Supplementary Table 1)[34]. As we expected, around 90% reads precipitated by H3K27me3 antibody were

332 mapped to *B. taurus* genome, while H3K4me3 were mapped relatively low percentage (32.18–63.12%). This

333 is because H3K4me3 antibodies successfully precipitated marks of both *T. annulata* and *B. taurus* histone 3

334 tails and the unmapped reads to either *B. taurus* or *D. melanogaster* genomes were mapped to the *T. annulata*

335 genome (data not shown). Peak calling were performed using Adaptive Local Threshold (ALT) equipped in

336 Easeq (windowsize:3000bp for H3K27me3, 1500bp for H3K4me3, p-value:1E-5, false discovery rate

337 (FDR):1E-5, Log2fold diff :2, merge within:100bp) or MACS2 algorithm and subsequently annotated to *B.*

338 *taurus* transcripts (UMD3.1.1, n=44681)[65,66]. For clustering of each Chip-seq, we performed MACS2 peak

339 call and clustering of all data by Bioconducter DiffBind package[67]. DiffBind clustering of peaks and high

340 Pearson's correlations coefficient (r >0.95) between 2 biological replicates of each macrophage and antibody

341 indicated that the ChIP-seq had worked correctly (Supplementary Fig. S1 b and c). We calculated H3K27me3

342 and H3K4me3 ratio of quantified value of each gene around +/- 2 kb from TSS between virulent and

343 attenuated cell. Venn diagrams of the histone mark positive transcripts between virulent and attenuated

344 macrophages were generated by R. All raw data of ChIP-seq and RNAseq have been uploaded to European

345 Nucleotide Archive (www.ebi.ac.uk/ena/) under the Study accession number PRJEB52136.

346 **Fibronectin binding assay**

347 Virulent and attenuated macrophage were treated with DMSO, 1μM UNC1999 or 1μM UNC2400 (inactive

348 analog) for 10 days[37,38]. Treated macrophages were load fibronectin coated plate and incubated for 1 h at 37

349 °C. Bound cells after PBS wash were stained by Violet blue and lysed by lysis buffer containing Triton X-

350 100. Number of the cells were quantified by absorbance of 595 nm.

351 **Dissemination of *T. annulata*-transformed macrophages in immune-deficient mice**

352 *T. annulata*-transformed virulent and attenuated macrophage lines were treated *in vitro* for ten days with

353 DMSO or 1μM UNC1999, as described above. The macrophages (10^6 in 200 μl PBS) were then injected

354 subcutaneously into right flank region of 'alymphoid' Rag2/γC double-deficient (T-, B-, NK-) mice and

355 surveyed for 3 weeks[35]. Four groups each containing five age and sex matched mice were defined: two

356 treatment groups including virulent/attenuated Ode treated with EZH2 inhibitor and two control groups

357 including virulent/attenuated Ode treated only with drug vehicle (solvent). During the three-week study

358 period, mice in the treatment groups were orally administered with UNC1999 (100 mg/kg/day) dissolved in

359 solution of Tween® 80 (Sigma-Aldrich, Germany) and carboxymethyl cellulose sodium salt (Sigma life

360 science, USA) to facilitate oral gavage. The control mice received 100 µl of solvent per day. At the end of

361 study, mice were humanely sacrificed and organs were dissected and kept in PBS at -20°C.

362 **Absolute quantification of *T. annulata*-infected cells in mice tissues**

363 A single copy *T. annulata* gene (apical merozoite antigen 1, TA02980) was cloned into pJET 1.2/blunt

364 cloning vector using CloneJET PCR Cloning Kit (Thermo Fisher Scientific). To measure the load of *T.*

365 *annulata*-infected macrophages in each tissue, quantitative PCR technology were applied to genomic DNA

366 extracted from mouse tissue (QIAmp DNA mini kit). Quantification were done based on the methodology

367 described elsewhere[68]. Briefly, a standard curve was generated from crossing points (Cp) measured from serial

368 dilutions of pJET-ama plasmid construct with known plasmid copy numbers using qPCR assay. The Cps from

369 1 ng DNA of each tissue sample were used to estimate parasite gene copy numbers based on the equation

370 derived from plotted data of the standard curve graph.

371 **Library preparation and sequencing**

372 We maintained virulent and attenuated macrophages with 1 µM PRC2 inhibitor for 10 days and collected 2.5

373 $\times 10^6$ cells of which total RNA were extracted by mirVana miRNA isolation Kit (Thermo Fisher Scientific,

374 catalogue number AM1560) according to the manufacturer protocol. Strand-specific RNA-sequencing

375 (ssRNA-seq) libraries were prepared using the Illumina Truseq Stranded mRNA Sample Preparation Kit

376 (Illumina, catalogue number RS-122-2101) following the manufacturer's instructions. Briefly, 1ug of total

377 RNA was used to purify mRNA using poly-T oligo-attached magnetic beads. mRNA was then fragmented
378 and cDNA was synthesized using SuperScript III reverse transcriptase (Thermo Fisher Scientific, catalogue
379 number 18080044), followed by adenylation on the 3' end, barcoding and adapter ligation. The adapter ligated
380 cDNA fragments were then enriched and cleaned with Agencourt Ampure XP beads (Agencourt, catalogue
381 number A63880). Libraries validation was conducted using the 1000 DNA kit on 2100 Bioanalyzer (Agilent
382 Technologies, catalogue number 5067-1504) and quantified using Qubit (Thermo Fisher Scientific, catalogue
383 number Q32850). ssRNA libraries were sequenced on Illumina Hiseq4000.

384 **RNA seq analysis**

385 All reads are paired by timmmomatic and mapped to *Bos taurus* UMD.3.1 genome by HISAT2[69]. BAM files
386 converted by Samtools, as described above and were processed by HTSeq-count tools[70] to quantify mapped
387 reads on each gene. We obtained a DEGs lists among each group with logFC > ±1 and padj < 0.05 using
388 separately EdgeR and Limma of NetworkAnalyst or TCC-GUI[71,72] and made intersections of these two lists to
389 identify more stringent DEGs. Treemap of Gene ontology analysis were visualized by Revigo[73].

390 **Gene expression measurements by qRT-PCR**

391 Total RNA was extracted from cells using RNAeasy® plus mini kit (QIAGEN). Complementary DNA
392 (cDNA) synthesis was done by using 1 µg RNA as template and the GoScript™ reverse transcriptase kit
393 (Promega, Cat. No. A5001, USA), in 20 µl reaction volume according to the instructions manual. To perform
394 qRT-PCR target sequences were amplified in a SYBR green PCR master mix (ThermoFisher Scientific, Cat.
395 No. 4309155) mixed with diluted cDNA (1:20), double distilled water and primers. The PCR was run in

LightCycler® 480 instrument (Roche) and results analysed in Microsoft Excel. Finally, the $2^{-\Delta\Delta CT}$ methodology was employed to estimate relative gene expression levels[74]. The expression of Bovine GAPDH was used as the internal control for normalization. Graphs were prepared in GraphPad Prism V 8.4.0.

Ethics Statement

A detailed protocol (number 12-26) describing the above mice experiments was first submitted to and approved (number CEEA34.GL.03312) by the ethics committee for animal experimentation at the University of Paris-Descartes. The university ethics committee is registered with the French National Ethics Committee for Animal Experimentation that itself is registered with the European Ethics Committee for Animal Experimentation. The right to perform the mice experiments was obtained from the French National Service for the Protection of Animal Health and satisfied the animal welfare conditions defined by laws (R214-87 to R214-122 and R215-10) and GL was responsible for all experiment as he holds the French National Animal Experimentation permit with the authorization number (B-75-1249).

1. Rashid, M. *et al.* Economic Significance of Tropical Theileriosis on a Holstein Friesian Dairy Farm in Pakistan. *The Journal of parasitology* **104**, 310–312 (2018).

2. Nene, V. *et al.* The biology of Theileria parva and control of East Coast fever - Current status and future trends. *Ticks and Tick-borne Diseases* **7**, 549–564 (2016).

3. Mukhebi, A. W., Perry, B. D. & Kruska, R. Estimated economics of theileriosis control in Africa. *Prev. Vet. Med.* **12**, 73–85 (1992).

4. Nene, V. & Morrison, W. I. Approaches to vaccination against Theileria parva and Theileria annulata. *Parasite Immunol.* **38**, 724–734 (2016).

5. Mhadhbi, M. *et al.* In vivo evidence for the resistance of Theileria annulata to buparvaquone. *Veterinary Parasitology* **169**, 241–247 (2010).

6. Sharifiyazdi, H., Namazi, F., Oryan, A., Shahriari, R. & Razavi, M. Point mutations in the Theileria annulata cytochrome b gene is associated with buparvaquone treatment failure. *Veterinary Parasitology* **187**, 431–435 (2012).

7. Tretina, K., Gotia, H. T., Mann, D. J. & Silva, J. C. Theileria-transformed bovine leukocytes have cancer hallmarks. *Trends Parasitol.* **31**, 306–314 (2015).

8. Villares, M. *et al.* Theileria parasites sequester host eIF5A to escape elimination by host-mediated autophagy. *Nat. Commun.* **15**, 2235 (2024).

9. Heussler, V. T. *et al.* Hijacking of host cell IKK signalosomes by the transforming parasite Theileria. *Science (New York, N.Y.)* **298**, 1033–1036 (2002).

10. Nigro, J. M. *et al.* Mutations in the p53 gene occur in diverse human tumour types. *Nature* **342**, 705–708 (1989).

11. Haller, D. *et al.* Cytoplasmic sequestration of p53 promotes survival in leukocytes transformed by Theileria. *Oncogene* **29**, 3079–3086 (2010).

12. Lizundia, R. *et al.* c-Jun NH2-terminal kinase/c-Jun signaling promotes survival and metastasis of B lymphocytes transformed by Theileria. *Cancer Research* **66**, 6105–6110 (2006).

13. Lizundia, R. *et al.* The JNK/AP-1 pathway upregulates expression of the recycling endosome rab11a gene in B cells transformed by Theileria. *Cellular Microbiology* **9**, 1936–1945 (2007).

14. Latré De Laté, P. *et al.* Theileria highjacks JNK2 into a complex with the macroschizont GPI (GlycosylPhosphatidylInositol)-anchored surface protein p104. *Cellular Microbiology* **21**, (2019).

15. Marsolier, J. *et al.* Theileria parasites secrete a prolyl isomerase to maintain host leukocyte transformation. *Nature* **520**, 378–382 (2015).

16. Dessauge, F., Lizundia, R., Baumgartner, M., Chaussepied, M. & Langsley, G. Taking the Myc is bad for Theileria. *Trends in parasitology* **21**, 377–385 (2005).

17. Dessauge, F. *et al.* c-Myc activation by Theileria parasites promotes survival of infected B-lymphocytes. *Oncogene* **24**, 1075–1083 (2005).

18. Shiels, B. *et al.* Alteration of host cell phenotype by Theileria annulata and Theileria parva: mining for manipulators in the parasite genomes. *International journal for parasitology* **36**, 9–21 (2006).

19. Chaussepied, M. *et al.* TGF-b2 induction regulates invasiveness of Theileria-transformed leukocytes and disease susceptibility. *PLoS Pathog.* **6**, e1001197 (2010).

20. Haidar, M. *et al.* TGF-beta2 induces Grb2 to recruit PI3-K to TGF-RII that activates JNK/AP-1-signaling and augments invasiveness of Theileria-transformed macrophages. *Scientific reports* **5**, 15688 (2015).

21. Haidar, M., Echebli, N., Ding, Y., Kamau, E. & Langsley, G. Transforming growth factor ??2 promotes transcription of COX2 and EP4, leading to a prostaglandin E<inf>2</inf>-driven autostimulatory loop that enhances virulence of Theileria annulata-transformed macrophages. *Infection and Immunity* **83**, 1869–1880 (2015).

22. Bowman, G. D. & Poirier, M. G. Post-translational modifications of histones that influence nucleosome dynamics. *Chem. Rev.* **115**, 2274–2295 (2015).

23. Ruthenburg, A. J., Allis, C. D. & Wysocka, J. Methylation of Lysine 4 on Histone H3: Intricacy of Writing and Reading a Single Epigenetic Mark. *Molecular Cell* **25**, 15–30 (2007).

24. Cock-Rada, A. M. *et al.* SMYD3 promotes cancer invasion by epigenetic upregulation of the metalloproteinase MMP-9. *Cancer Research* **72**, 810–820 (2012).

25. Margueron, R. & Reinberg, D. The Polycomb complex PRC2 and its mark in life. *Nature* **469**, 343–349 (2011).

26. Aloia, L., Di Stefano, B. & Di Croce, L. Polycomb complexes in stem cells and embryonic development. *Development (Cambridge)* **140**, 2525–2534 (2013).

27. Wassef, M. & Margueron, R. The Multiple Facets of PRC2 Alterations in Cancers. *Journal of molecular biology* **429**, 1978–1993 (2017).

28. Baylis, H. A., Megson, A. & Hall, R. Infection with Theileria annulata induces expression of matrix metalloproteinase 9 and transcription factor AP-1 in bovine leucocytes. *Molecular and Biochemical Parasitology* **69**, 211–222 (1995).

29. Hall, R. *et al.* Mechanism(s) of attenuation of Theileria annulata vaccine cell lines. *Tropical medicine & international health : TM & IH* **4**, A78-84 (1999).

30. Nardelli, S. C. *et al.* The histone code of Toxoplasma gondii comprises conserved and unique posttranslational modifications. *mBio* **4**, 1–12 (2013).

31. Trelle, M. B., Salcedo-Amaya, A. M., Cohen, A. M., Stunnenberg, H. G. & Jensen, O. N. Global histone analysis by mass spectrometry reveals a high content of acetylated lysine residues in the malaria parasite Plasmodium falciparum. *Journal of Proteome Research* **8**, 3439–3450 (2009).

32. Karmodiya, K. *et al.* A comprehensive epigenome map of Plasmodium falciparum reveals unique mechanisms of transcriptional regulation and identifies H3K36me2 as a global mark of gene suppression. *Epigenetics and Chromatin* **8**, 1–18 (2015).

33. Coetzee, N. *et al.* Quantitative chromatin proteomics reveals a dynamic histone post-translational modification landscape that defines asexual and sexual Plasmodium falciparum parasites. *Scientific Reports* **7**, 1–12 (2017).

34. Orlando, D. A. *et al.* Quantitative ChIP-Seq normalization reveals global modulation of the epigenome. *Cell Reports* **9**, 1163–1170 (2014).

35. Rchiad, Z. *et al.* Novel tumour suppressor roles for GZMA and RASGRP1 in Theileria annulata-transformed macrophages and human B lymphoma cells. *Cell. Microbiol.* **22**, e13255 (2020).

36. Roach, T. *et al.* CD45 regulates Src family member kinase activity associated with macrophage integrin-mediated adhesion. *Curr. Biol.* **7**, 408–417 (1997).

37. Konze, K. D. *et al.* An orally bioavailable chemical probe of the lysine methyltransferases EZH2 and EZH1. *ACS Chemical Biology* **8**, 1324–1334 (2013).

38. Xu, B. *et al.* Selective inhibition of EZH2 and EZH1 enzymatic activity by a small molecule suppresses MLL- rearranged leukemia. *Blood* **125**, 346–357 (2015).

39. Zabkiewicz, C., Resaul, J., Hargest, R., Jiang, W. G. & Ye, L. Increased expression of follistatin in breast cancer reduces invasiveness and clinically correlates with better survival. *Cancer Genomics and Proteomics* **14**, 241–251 (2017).

40. Seachrist, D. D. *et al.* Follistatin is a metastasis suppressor in a mouse model of HER2-positive breast cancer. *Breast Cancer Research* **19**, 1–10 (2017).

41. Zhu, J. *et al.* Genome-wide chromatin state transitions associated with developmental and environmental cues. *Cell* **152**, 642–654 (2013).

42. Striepen, B., Jordan, C. N., Reiff, S. & van Dooren, G. G. Building the perfect parasite: cell division in apicomplexa. *PLoS Pathog.* **3**, e78 (2007).

43. Strom, A. R. *et al.* Phase separation drives heterochromatin domain formation. *Nature* **547**, 241–245 (2017).

44. Tatavosian, R. *et al.* Nuclear condensates of the Polycomb protein chromobox 2 (CBX2) assemble through phase separation. *Journal of Biological Chemistry* **294**, 1451–1463 (2019).

45. Plys, A. J. *et al.* Phase separation of polycomb-repressive complex 1 is governed by a charged disordered region of CBX2. *Genes and Development* **33**, 799–813 (2019).

46. Metheni, M. *et al.* The level of H_2O_2 type oxidative stress regulates virulence of Theileria-transformed leukocytes: Oxidative stress, glycolysis andTheileriainfection. *Cell. Microbiol.* **16**, 269–279 (2014).

47. Niu, Y., DesMarais, T. L., Tong, Z., Yao, Y. & Costa, M. Oxidative stress alters global histone modification and DNA methylation. *Free Radic. Biol. Med.* **82**, 22–28 (2015).

48. Hakimi, M.-A., Olias, P. & Sibley, L. D. Toxoplasma Effectors Targeting Host Signaling and Transcription. *Clinical microbiology reviews* **30**, 615–645 (2017).

49. Xue, B., Dunker, A. K. & Uversky, V. N. Orderly order in protein intrinsic disorder distribution: disorder in 3500 proteomes from viruses and the three domains of life. *Journal of biomolecular structure & dynamics* **30**, 137–149 (2012).

50. Larcombe, S. D. *et al.* Susceptibility to disease (tropical theileriosis) is associated with differential expression of host genes that possess motifs recognised by a pathogen DNA binding protein. *PLoS One* **17**, e0262051 (2022).

51. Durrani, Z. *et al.* A parasite DNA binding protein with potential to influence disease susceptibility acts as an analogue of mammalian HMGA transcription factors. *PLoS One* **18**, e0286526 (2023).

52. Brühlmann, F. *et al.* TurboID mapping reveals the exportome of secreted intrinsically disordered proteins in the transforming parasite Theileria annulata. *MBio* e0341223 (2024) doi:10.1128/mbio.03412-23.

53. Lu, C. *et al.* Histone H3K36 mutations promote sarcomagenesis through altered histone methylation landscape. *Science* **352**, 844–849 (2016).

54. Souroullas, G. P. *et al.* An oncogenic Ezh2 mutation induces tumors through global redistribution of histone 3 lysine 27 trimethylation. *Nat. Med.* **22**, 632–640 (2016).

55. Rolando, M. *et al.* Legionella pneumophila effector RomA uniquely modifies host chromatin to repress gene expression and promote intracellular bacterial replication. *Cell Host and Microbe* **13**, 395–405 (2013).

56. Kamhawi, S. & Serafim, T. D. Leishmania: A Maestro in Epigenetic Manipulation of Macrophage Inflammasomes. *Trends in parasitology* **36**, 498–501 (2020).

57. Afrin, F., Khan, I. & Hemeg, H. A. Leishmania-host interactions-an epigenetic paradigm. *Frontiers in Immunology* **10**, 1–9 (2019).

58. Lecoeur, H. *et al.* Targeting Macrophage Histone H3 Modification as a Leishmania Strategy to Dampen the NF-κB/NLRP3-Mediated Inflammatory Response. *Cell Reports* **30**, 1870-1882.e4 (2020).

59. Braun, L. *et al.* The Toxoplasma effector TEEGR promotes parasite persistence by modulating NF-κB signalling via EZH2. *Nature microbiology* **4**, 1208–1220 (2019).

60. Adamson, R. & Hall, R. A role for matrix metalloproteinases in the pathology and attenuation of Theileria annulata infections. *Parasitology today (Personal ed.)* **13**, 390–393 (1997).

61. Shiels, B. R., McDougall, C., Tait, A. & Brown, C. G. Identification of infection-associated antigens in Theileria annulata transformed cells. *Parasite immunology* **8**, 69–77 (1986).

62. Langmead, B. & Salzberg, S. Bowtie2. *Nature methods* **9**, 357–359 (2013).

63. Li, H. *et al.* The Sequence Alignment/Map format and SAMtools. *Bioinformatics* **25**, 2078–2079 (2009).

64. Lerdrup, M., Johansen, J. V., Agrawal-Singh, S. & Hansen, K. An interactive environment for agile analysis and visualization of ChIP-sequencing data. *Nature structural & molecular biology* **23**, 349–357 (2016).

65. Zhang, Y. *et al.* Model-based analysis of ChIP-Seq (MACS). *Genome Biology* **9**, (2008).

66. Stark R and Brown, G. DiffBind: differential binding analysis of ChIP-Seq peak datatle. 1–29 (2016).

67. Gotia, H. T. *et al.* Absolute quantification of the host-To- Parasite DNA ratio in theileria parva- Infected lymphocyte cell lines. *PLoS ONE* **11**, 1–13 (2016).

68. Kim, D., Langmead, B. & Salzberg, S. L. HISAT: a fast spliced aligner with low memory requirements. *Nature methods* **12**, 357–360 (2015).

69. Anders, S., Pyl, P. T. & Huber, W. HTSeq-A Python framework to work with high-throughput sequencing data. *Bioinformatics* **31**, 166–169 (2015).

70. Xia, J., Benner, M. J. & Hancock, R. E. W. NetworkAnalyst - Integrative approaches for protein-protein interaction network analysis and visual exploration. *Nucleic Acids Research* **42**, 167–174 (2014).

71. Su, W., Sun, J., Shimizu, K. & Kadota, K. TCC-GUI: a Shiny-based application for differential expression analysis of RNA-Seq count data. *BMC Res. Notes* **12**, 133 (2019).

72. Supek, F., Bošnjak, M., Škunca, N. & Šmuc, T. Revigo summarizes and visualizes long lists of gene ontology terms. *PLoS ONE* **6**, (2011).

73. Livak, K. J. & Schmittgen, T. D. Analysis of relative gene expression data using real-time quantitative PCR and the 2(-Delta Delta C(T)) Method. *Methods* **25**, 402–408 (2001).

Author Contributions

TS performed all wet-bench experiments, ChIPseq bioinformatic analyses and wrote the manuscript with editorial inputs from **AP**, **MW** and **GL**. **ST** performed all mouse experiments including estimation of tumor dissemination and qRT-PCR analysis. **ZR** made the RNAseq libraries that were bioinformatically analyzed by **TS**, **HRA**, **AK** and **TM**. The study was conceived by **MW** and **GL** and supported by a joint grant awarded to **AP** and **GL**.

Acknowledgements

TS and **ST** acknowledge a LabEx ParaFrap postdoctoral fellowship and **GL** acknowledges ANR-11-LABX-0024 support and core funding from INSERM and the CNRS. **GL** and **AP** acknowledge financial support received from KAUST in form of a joint (OCRF-20146CRG4) grant and **AP** a BAS/1/1020-01-01 grant. We thank Raphael Margueron at the Curie Institute for help performing ChIPseq experiments; the Next Generation Sequencing Platform at the Curie Institute for ChIP sequencing, and members of the KAUST

Bioscience Core Laboratory (BCL) for generating the raw RNAseq datasets. We also thank Axel Martinelli at Hokkaido University for instruction on RNAseq analysis and Mads Lerdrup at the University of Copenhagen for guidance on ChIPseq analysis by EaSeq.

408 **Figure legends**

409 **Fig. 1. Localization of H3K27me3 and H3K4me3 marks in *Theileria*-infected virulent and attenuated**

410 **macrophages**

411 (a) Amino acid sequence alignment of Histone H3 tail among Apicomplexan parasites and *Homo sapiens*.

412 TA07840 sequence is used for *Theileria annulata.* (b) Immunofluorescence staining with H3K27me3 and

413 H3K4me3 (green). The monoclonal p104 antibody labels a parasite surface protein p104 (red) and DAPI

414 stained nuclei (blue). Lysin 27 is not tri-methylated in histone tails of *T. annulata* and H3K27me3 antibodies

415 stained only host nuclei. Tri-methylation on lysin 4 is conserved between *T. annulata* and bovine host nuclei.

416 Scale bar: 10 μm

417 **Fig. 2. Genome-wide H3K27me3 distribution dramatically changes in attenuated macrophages**

418 (a) Protein amounts of histone marks in both types of macrophage. Each band was normalized to H3 used as a

419 loading control. Relative intensity was described below each band. (b) 2D histogram visualized comparisons

420 of the two biological replicates of H3K27me3 and H3K4me3 ChIP-seq between virulent and attenuated

421 macrophages. Read counts found in the each gene of the virulent (on X-axis) and attenuated (on Y-axis)

422 macrophages are plotted. r value is the Pearson's correlations coefficient calculated. (c) Venn diagrams

423 showing common genes detected H3K27me3 and H3K4me3 peaks around TSS between virulent and

424 attenuated macrophages. Peaks of H3K27me3 and H3K4me3 were annotated to the *B. taurus* transcripts

425 (UMD3.1.1) and subsequently quantified around TSS +/- 2 kb by Easeq (52). (d) Tracks of H3K27me3 and
426 H3K4me3 superimposed signal (intensity on Y-axis) at all regions from the gene set of *Bos taurus* genome
427 (bosTau8). The X-axis represents within a 200% window centered on each gene with TSS and TTS.
428 Yellow/orange lines represent signals of virulent macrophages, whereas purple/black lines represent
429 attenuated macrophages.

430 **Fig. 3. H3K27me3 spreads non-specifically in attenuated macrophages**

431 (a) H3K27me3 and H3K4me3 heat maps around TSS +/- 10 kb of H3K27me3-positive genes either in virulent
432 or attenuated macrophages. Genes were sorted by the ratio of H3K27me3 signal log2 (Att/Vir). Cluster 1:
433 positive in virulent macrophages, Cluster 2: positive in attenuated macrophages, Cluster 3: positive in both
434 macrophages. Rep2 heat map is displayed. Tracks of H3K27me3 and H3K4me3 superimposed signal
435 (intensity on Y-axis) at the gene set of 3 cluster in virulent or attenuated macrophages. The X-axis represents
436 within a 200% window centered on each gene with TSS and TTS. Black lines represent signals of virulent
437 macrophages, whereas red lines represent attenuated macrophages. (b) Gene expression profile and DEGs of
438 each cluster. Average TPM values of each cluster were compared between virulent and attenuated
439 macrophages and p-values were calculated using Mann-Whitney U test. Within each cluster, the number of
440 down or up DEGs in attenuated *versus* virulent macrophages was determined using DESeq2 (FDR < 0.1, p-
441 value < 0.05, logFC > 1, logFC < -1). (c) Peaks of each mark on the representative genes in each cluster.

442

443 **Fig. 4. Spread H3K27me3 in attenuated macrophages lose its repressive function**

444 (a) PRC2 inhibitor UNC1999 specifically removed H3K27me3 marks, whereas the inactive analog UNC2400
445 didn't affect H3K27me3 marks. Both macrophages were treated with DMSO or PRC2 inhibitors for 10 days
446 and nuclear extract were prepared. (b) Fibronectin binding assay. PRC2 inhibitor treated cells were incubated
447 in a fibronectin coated well plate for 1 hour at 37 °C. Error bars show ± SD from 3 biological replicates. (c)
448 Dissemination of *T. annulate*-infected macrophages in immune-compromised Rag2/γC mice. Gene copy
449 number of parasites in each organ were obtained by absolute quantification correspond to *T. 36nnulate* ama-1
450 gene.

451 **Fig. 5. H3K27me3-mediated gene repression is dampened in attenuated macrophages**

452 (a) Number of DEGs (logFC > 1, logFC < -1, padj < 0.05) between virulent and attenuated macrophages
453 following PRC2 inhibitor treatment. (b) Venn diagram of common and uniquely upregulated genes in both
454 virulent (134 genes) and attenuated (50 genes) macrophages with the heatmaps of upregulated DEGs. (c)
455 Gene ontology analysis. Treemap were visualized by Revigo[73]. These pathways were specifically upregulated
456 upon PRC2 inhibitor treatment in each macrophage. (d) Heat map of the 21 common upregulated genes in
457 both macrophages upon UNC1999 treatment versus inactive analog UNC2400.

458 **Supplementary Fig. S1. Clustering of each ChIP-seq reads and scatter plot**

459 (a) Box plots represent the read counts on TSS around +/- 2kb of each gene obtained from H3K27me3 and
460 H3K4me3 ChIP-seq. ***, Wilcoxon rank-sum test p-value < 2.2e-16. (b) Clustering of each ChIP-seq
461 samples visualized by Bioconducter DiffBind package. (c) 2D Histogram of the virulent (on X-axis) and
462 attenuated (on Y-axis) macrophages parameters found in the gene set showing comparison of biological
463 replicates. r value is the Pearson's correlations coefficient calculated from input parameters.

464 **Supplementary Fig. S2. Peaks of H3K4me3 and H3K27me3 on representative 4 genes of the 21 common**
465 **upregulated genes relative to Figure 5**

466

467 **Supplementary Fig. S3. H3K27me3 and H3K4me3 profiles of upregulated genes upon PRC2 inhibitor**
468 **related treatment to Fig. 5b**

469 (a) H3K27me3 and H3K4me3 heat maps around TSS +/- 10 kb of 3 group of genes related to Fig.5b in
470 virulent or attenuated macrophages. Genes were sorted by the ratio of H3K27me3 signal log2 (Att/Vir). (b)
471 Tracks of H3K27me3 and H3K4me3 superimposed signal (intensity on Y-axis) at the gene set of 3 group of
472 genes related to Fig.5b in virulent or attenuated macrophages. The X-axis represents within a 200% window
473 centered on each gene with TSS and TTS. Black lines represent signals of virulent macrophages, whereas red
474 lines represent attenuated macrophages.

475 **Supplementary Fig. S4. H3K27me3 and H3K4me3 profiles of Down and Up DEGs in attenuated**

476 **macrophages.**

477 (a) H3K27me3 and H3K4me3 heat maps around TSS +/- 10 kb of Down and Up DEGs in attenuated

478 macrophages. (b) Tracks of H3K27me3 and H3K4me3 superimposed signal (intensity on Y-axis) at the gene

479 set of Down and Up DEGs in attenuated macrophages. The X-axis represents within a 200% window centered

480 on each gene with TSS and TTS. Black lines represent signals of attenuated macrophages, whereas red lines

481 represent virulent macrophages.

482

483 **Supplementary Fig. S5. *phf*19 expression in *Theileria*-infected virulent and attenuated macrophages**

qRT-PCR confirming significant downregulation of bovine PHF19 in attenuated Ode macrophages compared to their virulent counterparts. qRT-PCR data were normalized to bovine GAPDH. Two-tailed student's t-test was used to estimate significance. Mean fold-change in mRNA expression level ± standard errors shown. qRT-PCR results are representative of three independent experiments.

484

485 **Supplementary Table 1. Summary of ChIP-seq**

486 **Supplementary Table 2. List of differentially expressed genes corresponding to Fig 5b**

487 **Supplementary Table 3. List of primers for qRT-PCR**

Fig. 1

a

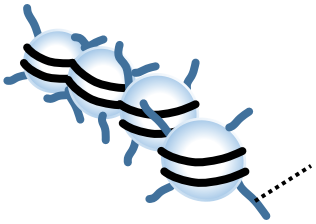

Histone H3 tail

	1 4 27 34
T. annulata	ARTKQTARKSTGGKAPRKQLASKAARKTAPVTGG
T. parva	ARTKQTARKSTGGKAPRKQLASKAARKTAPVTGG
T. orientalis	ARTKQTARKSTGGKAPRKQLASKAARKTAPVTGG
P. falciparum	ARTKQTARKSTAGKAPRKQLASKAARKSAPISAG
T. gondii	ARTKQTARKSTGGKAPRKQLASKAARKSAPMSGG
H. sapiens	ARTKQTARKSTGGKAPRKQLATKAARKSAPATGG

b

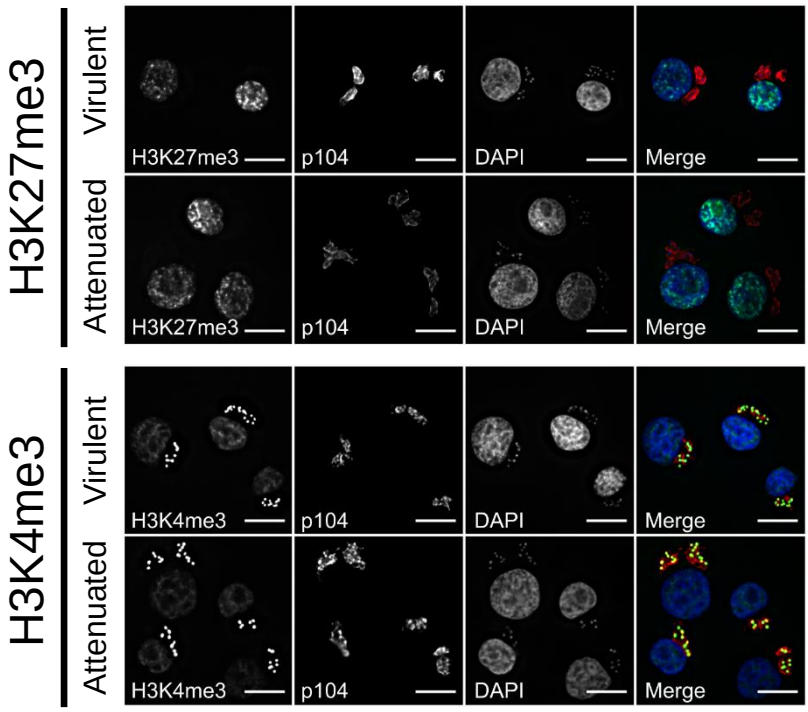

Fig. 2

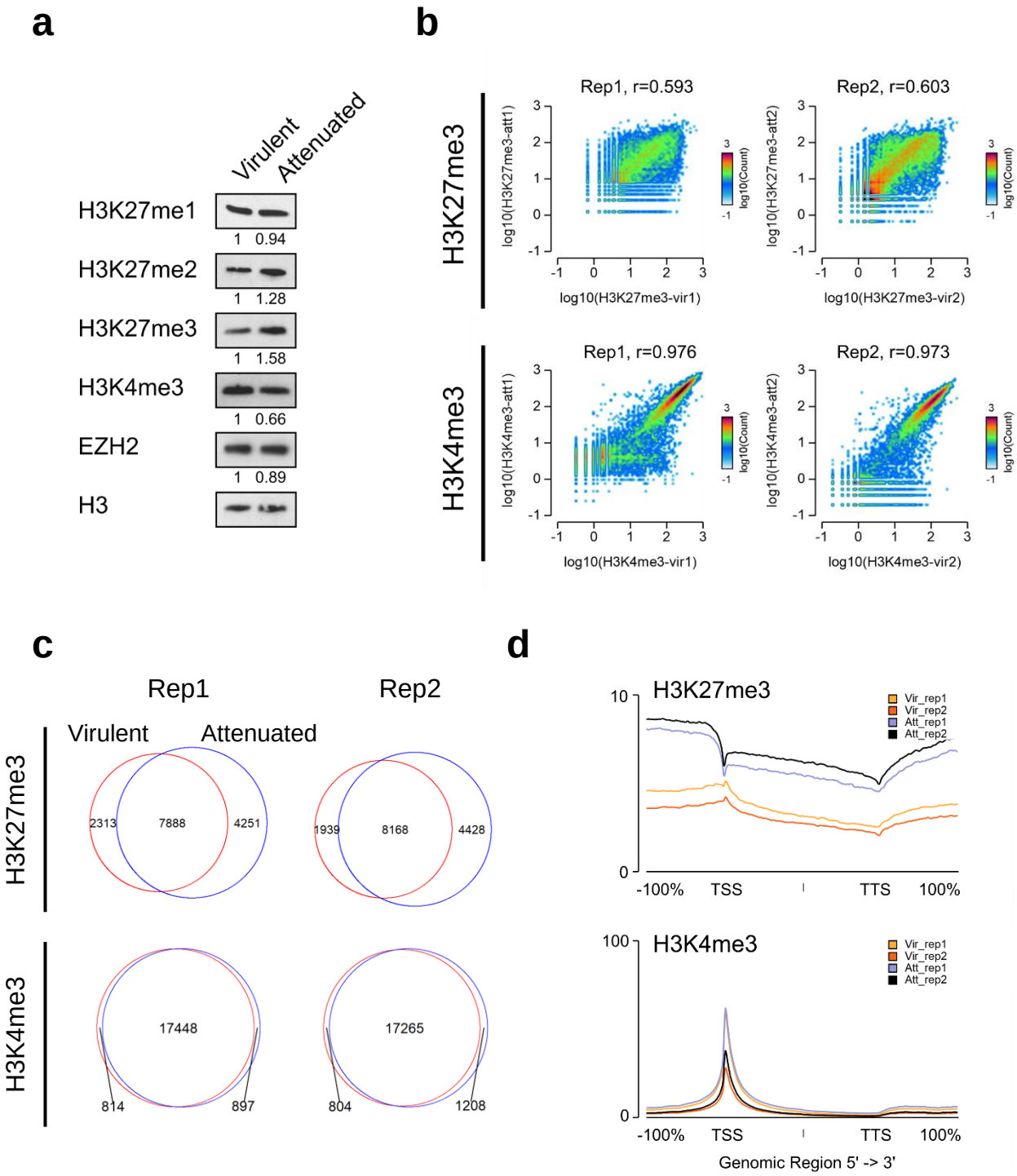
a
Virulent
Attenuated
H3K27me1
1 0.94
H3K27me2
1 1.28
H3K27me3
1 1.58
H3K4me3
1 0.66
EZH2
1 0.89
H3
b
H3K27me3
Rep1, r=0.593
log10(H3K27me3-att1)
log10(H3K27me3-vir1)
Rep2, r=0.603
log10(H3K27me3-att2)
log10(H3K27me3-vir2)
log10(Count)
H3K4me3
Rep1, r=0.976
log10(H3K4me3-att1)
log10(H3K4me3-vir1)
Rep2, r=0.973
log10(H3K4me3-att2)
log10(H3K4me3-vir2)
c
Rep1
Rep2
Virulent
Attenuated
H3K27me3
2313
7888
4251
1939
8168
4428
H3K4me3
17448
814
897
17265
804
1208
d
H3K27me3
Vir_rep1
Vir_rep2
Att_rep1
Att_rep2
-100%
TSS
TTS
100%
H3K4me3
Genomic Region 5' -> 3'

Fig. 3

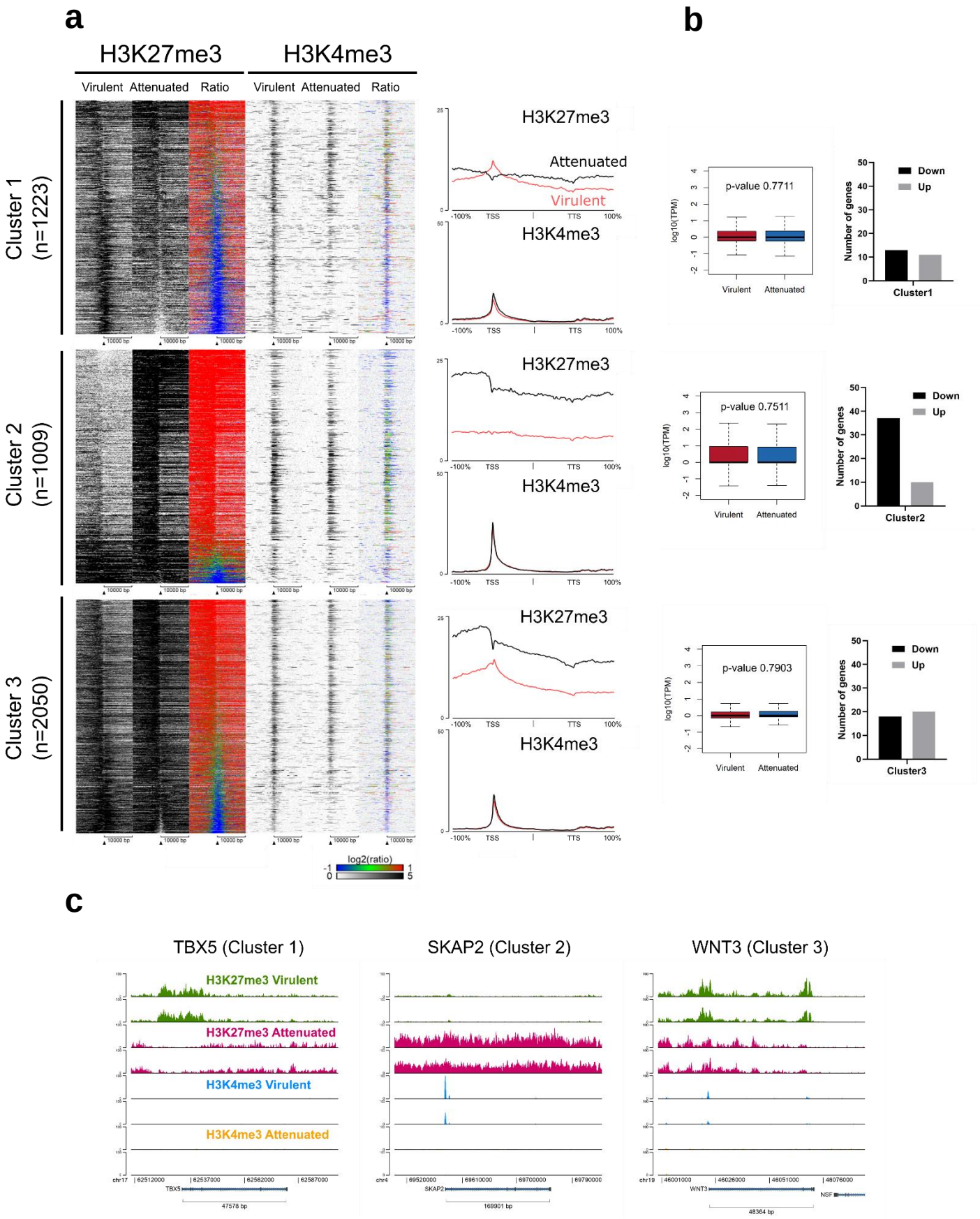
a
H3K27me3
H3K4me3
Virulent Attenuated Ratio
Virulent Attenuated Ratio
Cluster 1 (n=1223)
Cluster 2 (n=1009)
Cluster 3 (n=2050)
H3K27me3
Attenuated
Virulent
H3K4me3
-100% TSS TTS 100%
log2(ratio)
b
p-value 0.7711
p-value 0.7511
p-value 0.7903
log10(TPM)
Virulent Attenuated
Number of genes
Down
Up
Cluster1
Cluster2
Cluster3
c
TBX5 (Cluster 1)
SKAP2 (Cluster 2)
WNT3 (Cluster 3)
H3K27me3 Virulent
H3K27me3 Attenuated
H3K4me3 Virulent
H3K4me3 Attenuated
47578 bp
169901 bp
48364 bp

Fig. 4

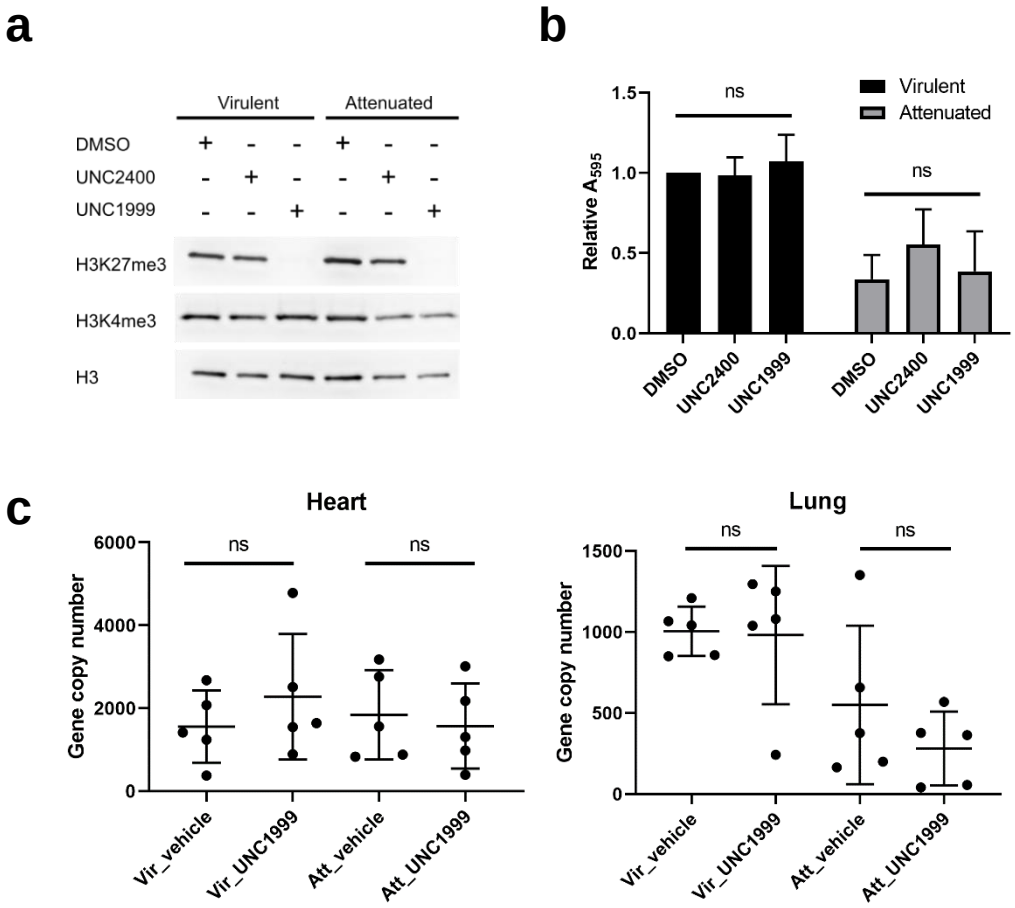
a
Virulent
Attenuated
DMSO
UNC2400
UNC1999
H3K27me3
H3K4me3
H3
b
Virulent
Attenuated
ns
ns
Relative A_{595}
1.5
1.0
0.5
0.0
DMSO
UNC2400
UNC1999
DMSO
UNC2400
UNC1999
c
Heart
Lung
ns
ns
Gene copy number
6000
4000
2000
0
1500
1000
500
Vir_vehicle
Vir_UNC1999
Att_vehicle
Att_UNC1999

Fig. 5

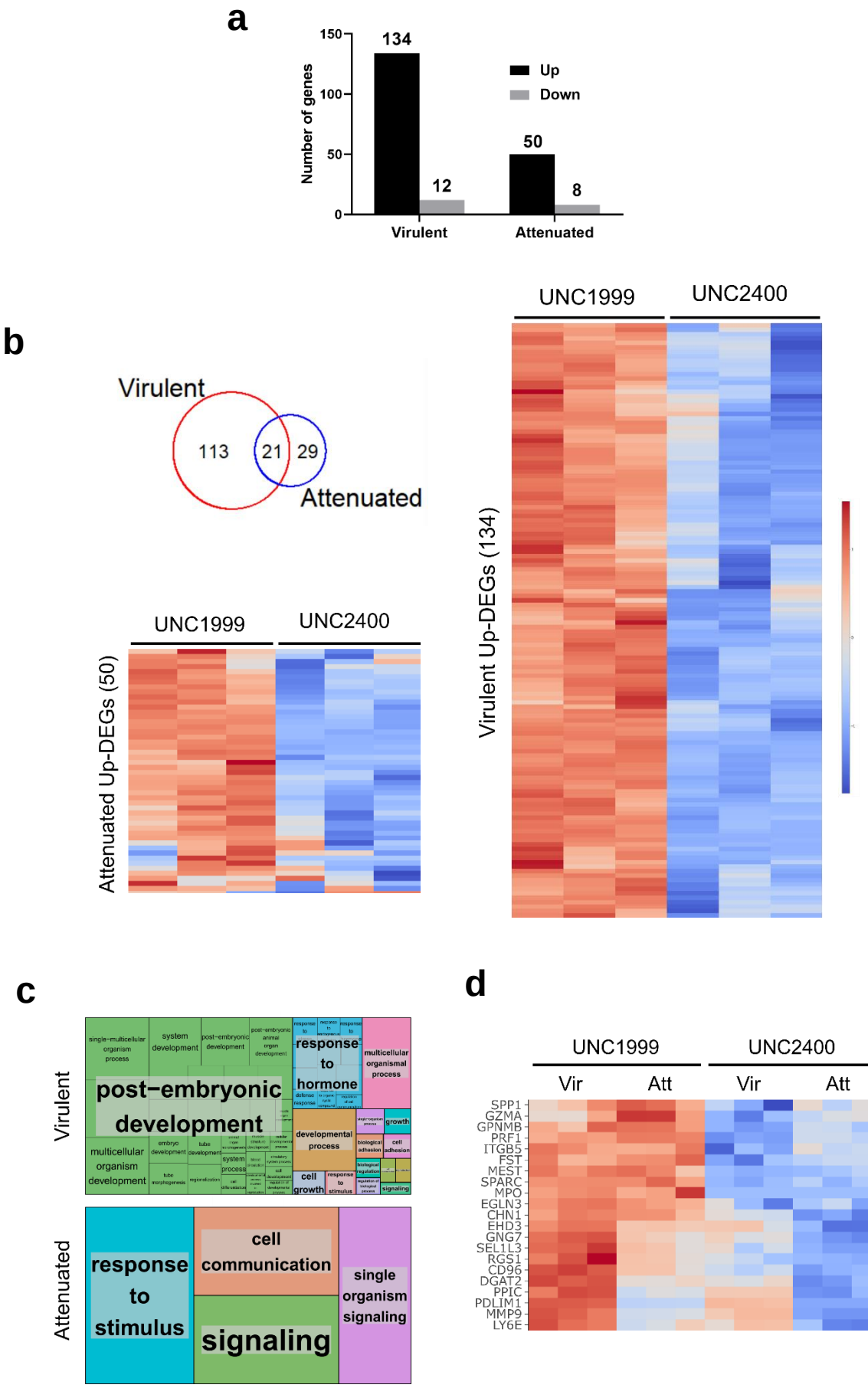
a
Number of genes
150
100
50
0
134
12
50
8
Up
Down
Virulent
Attenuated
b
Virulent
113
21
29
Attenuated
UNC1999
UNC2400
Attenuated Up-DEGs (50)
UNC1999
UNC2400
Virulent Up-DEGs (134)
c
Virulent
post−embryonic development
response to hormone
multicellular organismal process
developmental process
multicellular organism development
Attenuated
response to stimulus
cell communication
signaling
single organism signaling
d
UNC1999
UNC2400
Vir
Att
Vir
Att
SPP1
GZMA
GPNMB
PRF1
ITGB5
FST
MEST
SPARC
MPO
EGLN3
CHN1
EHD3
GNG7
SEL1L3
RGS1
CD96
DGAT2
PPIC
PDLIM1
MMP9
LY6E
1
0
-1
-2